

# Wrinkles of graphene on Ir(111): Macroscopic network ordering and internal multi-lobed structure

Marin Petrović,<sup>1,\*</sup> Jerzy T. Sadowski,<sup>2</sup> Antonio Šiber,<sup>1,3</sup> and Marko Kralj<sup>1,3</sup>

<sup>1</sup>*Institut za fiziku, Bijenička 46, 10000 Zagreb, Croatia*

<sup>2</sup>*Center for Functional Nanomaterials, Brookhaven National Lab, Upton, NY 11973, USA*

<sup>3</sup>*Center of Excellence for Advanced Materials and Sensing Devices,  
Institut za fiziku, Bijenička 46, 10000 Zagreb, Croatia*

The large-scale production of graphene monolayer greatly relies on epitaxial samples which often display stress-relaxation features in the form of wrinkles. Wrinkles of graphene on Ir(111) are found to exhibit a fairly well ordered interconnecting network which is characterized by low-energy electron microscopy (LEEM). The high degree of quasi-hexagonal network arrangement for the graphene aligned to the underlying substrate can be well described as a (non-Poissonian) Voronoi partition of a plane. The results obtained strongly suggest that the wrinkle network is frustrated at low temperatures, retaining the order inherited from elevated temperatures when the wrinkles interconnect in junctions which most often join three wrinkles. Such frustration favors the formation of multi-lobed wrinkles which are found in scanning tunneling microscopy (STM) measurements. The existence of multiple lobes is explained within a model accounting for the interplay of the van der Waals attraction between graphene and iridium and bending energy of the wrinkle. The presented study provides new insights into wrinkling of epitaxial graphene and can be exploited to further expedite its application.

## I. INTRODUCTION

Graphene is considered to be a promising material for various technological applications [1–4] due to its superior physical properties [5]. However, the desired intrinsic properties are often downgraded in chemically-synthesized graphene, including epitaxial graphene as the major large-scale source of the material, due to the structural defects in the honeycomb lattice (vacancies, pentagon-heptagon defects, grain boundaries) and out-of-plane deformations, where the latter can also be induced by the former [6]. Characteristic deformations in epitaxial graphene are wrinkles which form during the synthesis due to the lateral stress induced by the mismatch between thermal contraction of graphene and its substrate. In the literature, the out-of-plane deformations of graphene are sometimes also referred to as ripples, ridges or folds, depending on their size and structural details. In the present work, we do not make this distinction and by wrinkles we imply delaminated parts of graphene which can be thought of as one-dimensional (1D) objects at micron-scales, while forming a wrinkle network (WN) at larger scales as we demonstrate in the following. Wrinkles are found in graphene on metals [7–13], silicon carbide [14–16] as well as various samples based on transferred graphene [17–20]. Besides in graphene, wrinkling occurs in other types of layered materials [21, 22] and more generally in various systems, ranging from semiconductors [23] to soft matter and biological tissues [24].

The prominent role of wrinkles is that they affect the transport properties of graphene resulting, for example, in tunable transport gaps [25], reduction and anisotropy of electrical conductivity [18, 19] and a decrease of ther-

mal conductivity [26]. Moreover, highly curved surfaces of wrinkles exhibit increased chemical reactivity which has been predicted earlier [27] and was confirmed in experiments with oxygen etching [28, 29] and the growth of organic semiconductor structures [30]. Wrinkles are also important for the process of graphene intercalation. They facilitate the penetration of atoms across the graphene sheet either through defective regions characteristic for wrinkles interconnection sites [31, 32] or via temporary defects which may form due to an increased reactivity at curved graphene areas [33]. They also serve as pipelines for diffusion of already intercalated species [29, 34]. On a macroscopic scale, wrinkles play a significant role in the wettability and optical transmittance of graphene [35]. Therefore, a control over their macroscopic ordering accompanied by a systematic characterization is desirable for a successful technological implementation of graphene. Some efforts have already been made in the direction of wrinkle manipulation, e.g. modification of wrinkle orientation and length by the scanning tunneling microscopy (STM) tip for graphene on silicon carbide [15] or alteration of the wrinkle area density and orientation by selecting the appropriate substrate morphology for transferred graphene [17, 36].

From the published studies, typical heights and widths of wrinkles in epitaxial graphene are found to vary from below one and up to several tens of nanometers, depending on the substrate and graphene growth procedure [10, 11, 13, 15, 16, 18]. Internal substructure of wrinkles is often approximated by a single-lobed, semicircular shape [10, 16, 19]. However, other physical interactions involved in the wrinkle formation (e.g. van der Waals) may lead to the formation of more complex structures [18, 37].

Among epitaxially grown systems, graphene on iridium (111) surface [Gr/Ir(111)] is widely-explored due to the high structural quality [38] and almost intrinsic electronic properties [39, 40] of graphene. Up to now, experimental characterization of wrinkles of Gr/Ir(111) via low-energy electron microscopy (LEEM) and a simple model accounting for the wrinkle formation have been reported in the work of N'Diaye et al. [10]. There the authors focused on graphene islands and graphene containing several rotational domains with respect to the substrate. Similar samples were also used in the study of Loginova et al. [11]. Moreover, an x-ray standing wave studies revealed correlation between graphene coverage and its periodic buckling amplitude [41, 42] which is a consequence of the partial stress relaxation in graphene islands via their lateral expansion. Therefore, the structure of wrinkles is also expected to vary with graphene coverage. A detailed study on the relation between lattice parameters of graphene and iridium in a broad temperature interval revealed a hysteretic behavior of wrinkle formation and their flattening [43]. The same study showed that wrinkles on average relax  $\sim 2/3$  of the compressive stress imposed by iridium while  $\sim 1/3$  still remains in the graphene layer.

In this work, we are interested in wrinkles of the high-quality macroscopic graphene samples and hence we focus on the full monolayer of Gr/Ir(111) and refrain from the description of graphene islands and incomplete graphene layers. LEEM is used for the characterization of WN of Gr/Ir(111). The *in situ* imaging at elevated temperatures gives a detailed insight into the process of wrinkling. The WN is found to be well represented by an appropriate Voronoi partition of the plane with centroids constructed from the wrinkle positions. Analysis of STM measurements reveals that individual wrinkles have intriguing and complicated profiles. These are explained within a framework of a 1D model accounting for an interplay of different energies important for the wrinkle formation. Comparison of our model with experimental data strongly suggests that the wrinkles we observe are multi-lobed, i.e. that the graphene approaches and delaminates from iridium several times within the span of a single wrinkle.

## II. EXPERIMENTAL

Sample preparation and all experimental measurements were carried out *in situ* under ultra-high vacuum conditions. The Ir(111) single-crystal was cleaned by argon ion sputtering at room temperature at 1.5 keV ion energy, followed by oxygen glowing at 850 °C and annealing at 1200 °C. Graphene synthesis consisted of temperature programmed growth (TPG) followed by a chemical vapor deposition (CVD) which are known to yield full coverage of high quality graphene monolayer of uni-

form orientation [44] as confirmed by low-energy electron diffraction (LEED) after the synthesis. During TPG, ethylene was adsorbed on iridium at room temperature ( $1.33 \times 10^{-7}$  mbar for 45 s), followed by a flash to 1200 °C. During CVD, the sample was kept at 850 °C while being exposed to ethylene ( $1.33 \times 10^{-7}$  mbar for 900 s). The LEEM measurements were performed at the U5UA beamline of the NSLS synchrotron (Brookhaven National Laboratory) with an Elmitec LEEM III system. Sample temperature ( $T_s$ ), imaging electron energy ( $E_i$ ) and field of view (FOV) varied and are noted in figure captions. All LEEM images were recorded in the bright field mode. Spatial resolution of the microscope was  $\sim 10$  nm. STM experiments were performed in Zagreb using Specs Aarhus STM operating at room temperature. STM data was post-processed in WSxM software [45].

## III. RESULTS AND DISCUSSION

### A. Wrinkle network

Figure 1a shows a LEEM image of an area of Gr/Ir(111) where the dense-packed rows of Ir are aligned to the zig-zag directions of graphene lattice, referred to as R0 graphene [46]. Graphene wrinkles are identified as thick dark lines extending  $\sim 1 \mu\text{m}$  in length and forming a network. Thinner and more closely spaced wavy lines are steps of the iridium surface. It can be noted that wrinkles extend mainly in three directions rotated by an angle of  $\sim 60^\circ$ . As a consequence, wrinkle junctions most often involve three wrinkles separated by  $120^\circ$  rotation. This is directly confirmed in the Fourier transform (FT) of the background-subtracted Figure 1a, where a clear 6-fold symmetrical pattern is revealed, as shown in Figure 1b. The FT pattern consists of stripes and lacks spots which indicates that the separation between parallel wrinkles and their apparent thickness have a fairly broad distribution, but the directional preference is nevertheless clear. In order to perform a more quantitative analysis, radial sums of the FT are presented in a polar graph in Figure 1c. Again, the 6-fold symmetry is evident. After plotting the same data in a rectangular graph and fitting the six peaks with Gaussian curves (not shown), one can precisely determine the main directions in which the wrinkles extend. They are  $(53.5 \pm 0.3)^\circ$ ,  $(112.5 \pm 0.3)^\circ$  and  $(172.6 \pm 0.6)^\circ$  (cf. yellow lines in Figure 1d). The difference between these directions fits well to  $60^\circ$ , which agrees with the initial inspection of the LEEM image in Figure 1a. This kind of ordering along with the observation that wrinkle junctions contain mostly three wrinkles suggests that the wrinkles form a network composed dominantly of hexagons.

The exact orientation of the dense-packed atomic rows of the iridium surface, determined by precise movement of the sample along the high-symmetry directions dur-

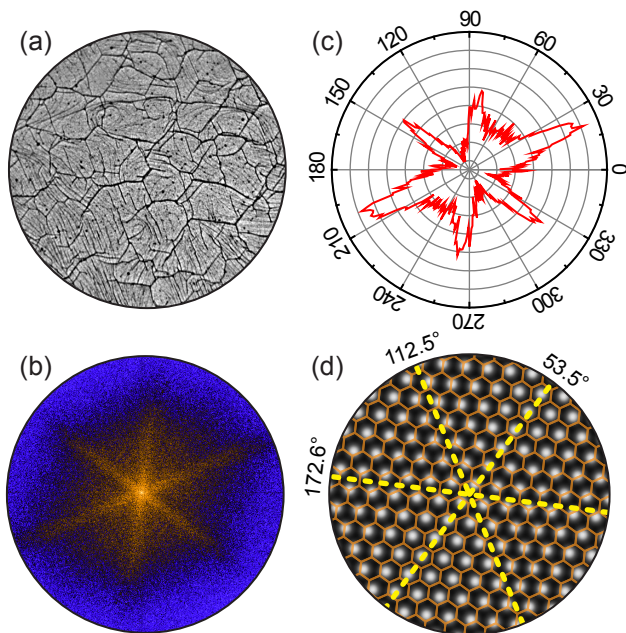


Figure 1. (a) LEEM image of Gr/Ir(111). Thick dark lines extending over the entire sample surface are graphene wrinkles, thinner wavy lines are iridium steps. FOV =  $9.3 \mu\text{m}$ ,  $E_i = 16 \text{ eV}$ ,  $T_s = 96^\circ\text{C}$ . (b) Fourier transform of image from (a). (c) Polar plot of radial sums extracted from (b). The red curve is plotted with a negative offset and in arbitrary units. (d) Arrangement of iridium atoms (gray spots), graphene (orange hexagons) and dominant directions of graphene wrinkle extension (yellow dashed lines).

ing LEEM imaging, is schematically illustrated in Figure 1d. In addition, yellow dashed lines mark three determined wrinkle-extending directions and a perfect coincidence between them and dense-packed rows of iridium is found. The shrinkage of iridium during cooldown after graphene synthesis can be simply described as a reduction of separation between adjacent atomic planes in the bulk and also atomic rows at the surface. From the observation of wrinkles directional ordering, it can be inferred that the shrinkage induces stress which is relaxed through the formation of wrinkles in the direction parallel to the atomic rows of iridium i.e. parallel to the zig-zag direction of graphene. Similar orientational locking was also proposed earlier for graphene flakes on iridium [10].

For a comparison to the preferred R0 graphene, orientation of the R30 graphene wrinkles was examined where the dense-packed rows of iridium are parallel to the armchair directions of graphene. Figure 2 shows the LEEM image of a boundary area between the R0 and R30 domains of graphene, as identified via micro-LEED patterns (upper panels), each exhibiting different LEEM reflectivity. The underlying Ir steps and wrinkles are present on both domains. The corresponding FT patterns from different graphene rotations are shown in bottom panels of Figure 2. Whereas the symmetry of the R0 transform is

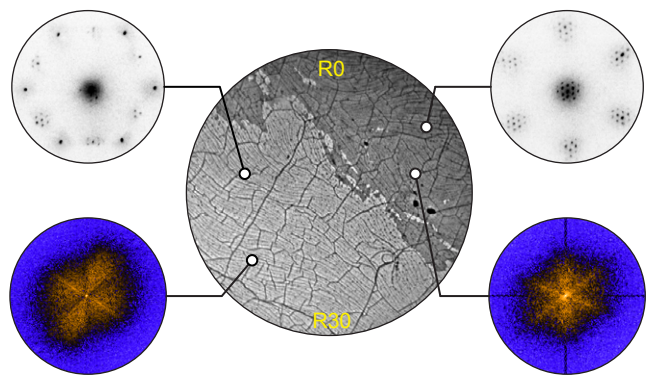


Figure 2. LEEM image of R0/R30 graphene boundary (center) with the corresponding micro-LEED diffraction patterns (upper panels) and Fourier transforms (bottom panels). FOV =  $14 \mu\text{m}$ ,  $E_i = 3.8 \text{ eV}$ ,  $T_s = 98^\circ\text{C}$ .

6-fold, the same as in Figure 1b, this is not the case for the R30 graphene where only two dominant, mutually perpendicular directions with a large angular spread are found. In principle, two distinct directions are enough for stress relaxation in two dimensions and the observation of three (two) directions in the R0 (R30) graphene calls for an explanation. We note that the graphene bending rigidity is essentially the same along the zig-zag and armchair directions in the range of bending radii (up to  $\sim 10 \text{ nm}$ ) relevant for wrinkling [47], ruling out the graphene lattice itself as a cause of the observed symmetry difference. It was argued in previous studies that the R30 graphene is more weakly bound to Ir as compared to the R0 graphene [48]. This suggests that (i) the R0 graphene is compelled to follow contraction of the substrate in each of the three equivalent directions defined by the (111) surface of FCC lattice and (ii) the R30 graphene does not have to keep track of the underlying Ir and is free to wrinkle in two approximately perpendicular directions. Apparently, the preference between the two wrinkling regimes is governed by the binding strengths of R0 and R30 graphene. However, the absolute orientation of the two wrinkling directions of R30 graphene is related to the substrate. It is visible in Figure 2 that some of the R30 wrinkles are parallel to Ir steps while others are perpendicular to them. Similar observations were made in the case of graphene on Pt(111), a system in which graphene is more weakly bound to the substrate as compared to the R0 Gr/Ir(111) [7, 29].

## B. Voronoi diagram approximation

On the basis of collected LEEM data, we can show that the WN on the R0 graphene can to a good extent be approximated by a Voronoi diagram (VD) i.e. a network obtained in a Voronoi tessellation of a plane [49]. The construction of a VD starts from a set of points

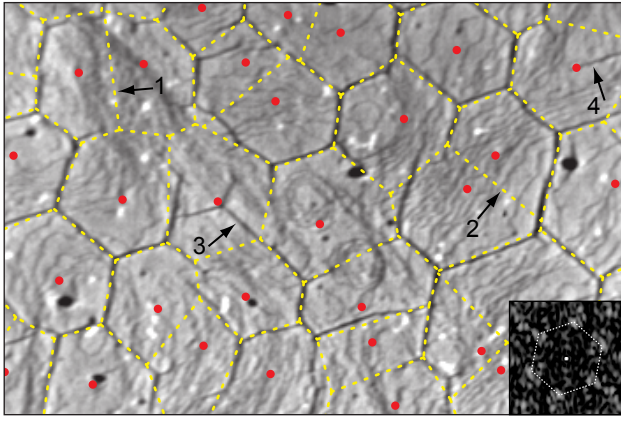


Figure 3. LEEM image of the graphene WN superimposed by the VD (yellow dashed lines) generated by red centroids. Arrows indicate several deviations of the diagram from the network. The inset shows Fourier transform of the centroids. Image size:  $(6.5 \times 4.3) \mu\text{m}^2$ ,  $E_i = 1.9 \text{ eV}$ ,  $T_s = 91 \text{ }^\circ\text{C}$ .

(called centroids) which divide the plane into cells (called Voronoi cells) associated to every centroid in a way that each cell contains only points that are closer to a given centroid than to any other. All Voronoi cells together constitute a VD. Figure 3 shows the recorded LEEM image of Gr/Ir(111) overlapped with the VD (yellow dashed lines) generated from a set of centroids marked as red dots. The positions of centroids can be determined from the WN by a simple geometrical construction applied to each cell of the network [50] (see Supplementary data for details). In the case of WN, large number of wrinkles coincide with the Voronoi cell borders with some minor exceptions. For example, the VD predicts the existence of wrinkles which are actually not there (cf. arrows 1 and 2) or the absence of wrinkles which are found at certain locations (cf. arrows 3 and 4). In spite of this, the VD approximation is satisfactory and is likely to get even better in cases when various defects on the iridium surface as well as iridium steps are suppressed to a minimum. In addition, shorter and smaller wrinkles are hard to resolve in LEEM and wrinkles in general can be mistaken for iridium steps and vice versa, which may deteriorate the approximation to some small extent.

It might seem at first that the spatial distribution of centroids in Figure 3 is random, but if that were the case wrinkles would not exhibit preference in their direction and the corresponding Fourier transforms would be isotropic, which is in contrast to what we observe. Moreover, Fourier transform of the centroids alone, displayed in the inset of Figure 3, exhibits hexagonal symmetry and indicates their quasi-periodic arrangement. In fact, a typical Voronoi cell of a WN is hexagonal, as can also be concluded from the analysis of Figure 1. It follows that the WN as well as the corresponding VD are networks of distorted hexagons similar to a honeycomb structure.

Based on these findings, WN can be simulated via construction of perfectly arranged honeycomb VD to which a specific amount of disorder has been introduced (see Figure S2 in the Supplementary data). VDs generated from a random distribution of centroids are referred to as Poisson-Voronoi diagrams and have been studied extensively [49, 51]. Expected values of various parameters (cell area, cell perimeter, number of edges etc.) of such diagrams have been calculated and simulated. These values are not expected to vary significantly for centroid distributions other than random [49], so they can be adopted for the characterization of the WN found for wrinkles in the R0 graphene. It is worth noting that the expected value of an angle at a typical wrinkle junction is  $120^\circ$ , as we also inferred from the data presented in Figure 1. One of the easiest quantities to obtain from LEEM is the number of wrinkle junctions per unit area,  $n_j$ . Once this number is known, expected values of several parameters of the network can be calculated from the theory of Poisson-Voronoi tessellation [49]. For the LEEM image in Figure 3, one finds  $n_j = 1.4 \mu\text{m}^{-2}$  and other derived parameters are given in Table I. For comparison, we also list the values of other parameters obtained from the experiment (Figure 3) which show good agreement with the theoretical predictions. Hence, by identifying the WN as a VD, one can easily estimate various parameters relevant for network's general description which in turn facilitates evaluation of the effect the wrinkles may have on the properties of graphene, e.g. electronic transport. Finally, the values given in the table are not universal but are expected to differ depending on the preparation parameters of graphene, especially the growth temperature.

### C. Dynamics of wrinkling

After the formation of 1 ML graphene and cooldown to room temperature, the sample was re-heated to  $650 \text{ }^\circ\text{C}$  and then slowly cooled down while LEEM images were being simultaneously recorded. Such experiment enabled the observation of disappearance and reappearance of individual wrinkles. In Figure 4a and b we show two areas of the sample recorded right before (frame 1) and after (frame 2) the appearance of several wrinkles during cooldown. By comparing frames 1 and 2, we deduce that the reflectivity of graphene surrounding the appearing wrinkles increases by 3% once the wrinkle is formed (see also the movie clip in the Supplementary data). This is even clearer in frame 3 where the difference of frames 2 and 1 is shown. This effect is discussed in the work of N'Diaye et al. [10] to be a result of a change in interference conditions of incoming and reflected electron waves. However, in the following we propose an additional mechanism for this local change of reflectivity.

In our experiment, LEEM images are recorded in



Table I. Parametrization of the WN. Parameters of the Poisson-Voronoi diagram (1<sup>st</sup> column), their mutual dependence (2<sup>nd</sup> column), values extracted from the LEEM image shown in Figure 3 (3<sup>rd</sup> column) and values calculated from the equations given in the second column (4<sup>th</sup> column). Calculations were performed based on the experimentally determined value  $n_j = 1.4 \mu\text{m}^{-2}$ .

parameter	relation to $n_j$	experimental value	calculated value
density of junctions, $n_j$	$n_j$	$1.4 \mu\text{m}^{-2}$	–
density of centroids	$\frac{n_j}{2}$	–	$0.7 \mu\text{m}^{-2}$
wrinkle length per unit area	$2\sqrt{\frac{n_j}{2}}$	$1.4 \mu\text{m}^{-1}$	$1.7 \mu\text{m}^{-1}$
area of a cell	$\frac{2}{n_j}$	–	$1.5 \mu\text{m}^2$
perimeter of a cell	$4\sqrt{\frac{2}{n_j}}$	–	$4.8 \mu\text{m}$
length of a single wrinkle	$\frac{2}{3}\sqrt{\frac{2}{n_j}}$	$(0.7 \pm 0.3) \mu\text{m}$	$0.8 \mu\text{m}$

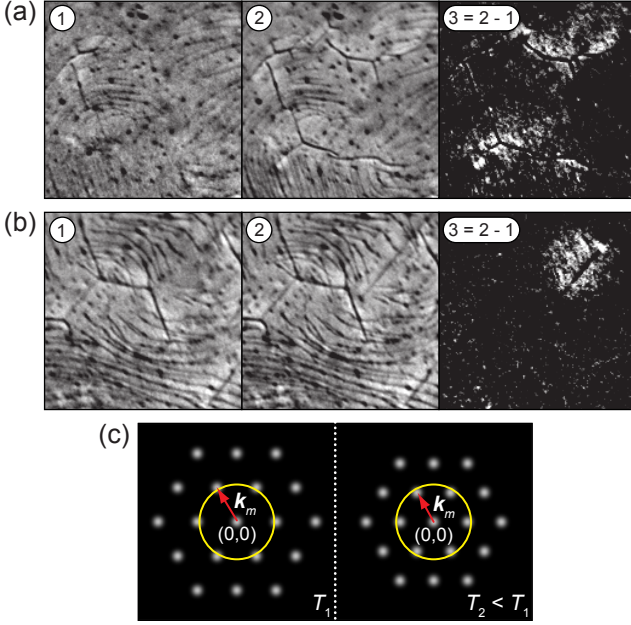


Figure 4. (a, b) LEEM micrographs,  $(3 \times 3) \mu\text{m}^2$  in size, showing two different areas in of Gr/Ir(111) right before (frame 1) and after (frame 2) wrinkle emergence. Frame 3 displays the difference  $2 - 1$ . (a) is recorded at  $350^\circ\text{C}$ , (b) at  $270^\circ\text{C}$ .  $E_i = 3.8 \text{ eV}$ . (c) An illustration of the origin of LEEM reflectivity changes upon wrinkle formation (see text for details). White spots represent  $(0,0)$  and moiré diffraction spots. Yellow circle indicates size of the contrast aperture used for LEEM imaging.  $\mathbf{k}_m$  is the moiré wave vector, its variation at temperatures  $T_1$  and  $T_2$  is exaggerated for clarity.

bright field mode at  $3.8 \text{ eV}$  electron energy and at such low energies only the  $(0,0)$  spot and a fraction of higher order moiré spots contribute to image formation (cf. Figure 4c). Furthermore, at the onset of wrinkle formation, the surrounding graphene lattice relaxes, leading to an increase of the graphene lattice parameter and consequently a decrease of the moiré wave vector module  $k_m$ . This brings moiré diffraction spots closer to the  $(0,0)$  spot by roughly 3% [43] (cf. Figure 4c). Hence, a decrease of  $k_m$  results in an increase of the fraction of moiré spots in-

tensity contributing to LEEM images. In other words, areas in LEEM images which become brighter after a wrinkle forms are areas where the graphene lattice is relaxed as compared to its surroundings. In this way graphene lattice relaxation can be directly observed in real space. This also indicates that the stress imposed on graphene is visibly relaxed only in the  $\sim 0.5 \mu\text{m}$  vicinity of the wrinkle and that graphene areas situated further away remain highly stressed, at least at elevated temperatures of several hundred degrees Celsius. The scenario of localized stress relaxation is supported by recent theoretical simulations showing that graphene stretching energy is reduced in the wrinkles' surroundings [52]. Upon further sample cooldown, the reflectivity (and hence graphene stress) in the entire LEEM field of view equalizes but still exhibits local variations which appear to be related to iridium surface steps. Similar relation between stress non-uniformity and substrate morphology has been observed for graphene on silicon carbide [53]. Finally, at room temperature when the surface is characterized by a fully formed WN, the reflectivity variations are diminished and indicate uniformity of stress in graphene.

Monitoring of the disappearance and reappearance of wrinkles in LEEM during re-heating enabled examination of wrinkle nucleation sites. Figures 5(a) and (b) show two LEEM images of the same area on the sample. Image (a) was recorded at  $247^\circ\text{C}$  during heating and image (b) at  $247^\circ\text{C}$  during cooling of the sample. In between, the sample temperature reached a maximum of  $650^\circ\text{C}$  when all wrinkles were flattened out. Re-heating cycles involve thermal drift of the sample, but prominent iridium features (such as a series of distinct circular terraces, cf. red arrow in Figure 5) enabled identification and observation of the same surface area for the given temperature. Comparison of the two images allows us to infer that some of the wrinkles reappeared at the same location (cf. white arrows in Figure 5) but many other formed at new positions which were wrinkle-free before re-heating (some of them marked by yellow arrows in Figure 5). The number of wrinkles in Figure 5b is apparently lower than in Figure 5a which is due to the hysteretic behavior of the wrinkle formation [43]. Additional wrinkles appear as the

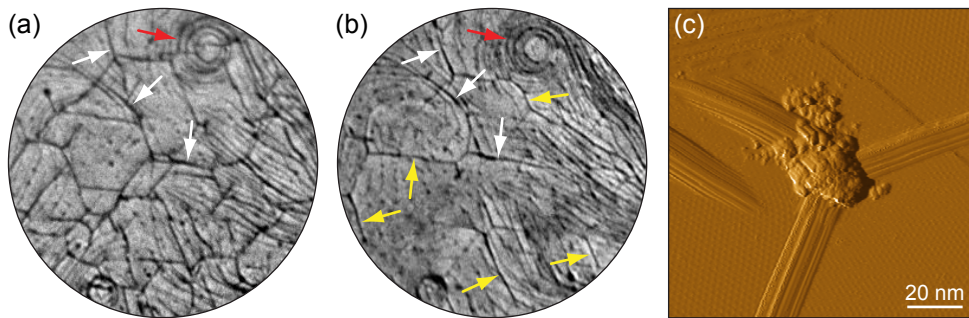


Figure 5. (a, b) LEEM images illustrating wrinkle pinning. Several graphene wrinkles are visible (a) at 247 °C during heating and (b) at 247 °C during cooling. Some of the wrinkles reappeared in the same locations (white arrows) while some formed in new locations (yellow arrows). Characteristic Ir terraces (red arrows) facilitate identification of the same surface area of the sample. FOV = 7.2  $\mu\text{m}$ ,  $E_i = 3.8$  eV. (c) STM image of the wrinkle junction anchored at leftover dirt particle (first derivative of the topography image). Tunneling voltage: 630 mV, tunneling current: 1.7 nA.

sample is further cooled down to room temperature, but due to mentioned thermal drift a more precise comparison for exactly the same surface area cannot be made. We also observe that new wrinkles often form at the endpoints of already existing ones and the whole process sometimes resembles to "crack" (wrinkle) propagation (see also the movie clip in the Supplementary data).

We conclude from our experiments that various structural features of graphene or iridium can anchor some of the wrinkles, serving as nucleation sites for their formation. However, many wrinkles are exempt from this. A typical wrinkle junction containing dirt particle, most likely a leftover from the crystal cleaning process, was characterized with STM and is shown in Figure 5c. Such sites are suitable for the nucleation of wrinkles due to the reduced binding of graphene to the substrate and a presumably large number of defects contained in the graphene lattice itself. If dirt particles are stable at elevated temperatures, they can anchor wrinkles i.e. they are preferred sites of wrinkle nucleation. This is in line with previous findings on graphene flakes where the authors claim that majority of wrinkles nucleate at defects, more precisely at heptagon-pentagon pairs [10].

#### D. Multi-lobed wrinkles

We now proceed to examine the features of individual wrinkles, in particular their widths and heights and the variation of graphene-iridium separation within a single wrinkle, i.e. the wrinkle profile. A simple, single-lobed profile is often considered, but one may examine more complicated profiles consisting of several consecutive lobes. Motivation for such profiles is found in the STM measurements (shown in Figure 5c and below, in Figure 7) and it is of interest to study the energetics of their formation. The energies of different profiles are compared using a simple *ansatz* for the profile shape which has been shown to accurately describe the compression-governed delamination of graphene [54]

and other thin films [55, 56]. The profile is represented by the cosine function of the amplitude  $A_m$  extending over  $m$  periods of length  $l_m$ , leading thus to  $m$  successive identical lobes. The total width of the profile is  $l_1$  (the width of a single-lobed wrinkle) for every  $m$ . The out-of-plane displacement of  $m$ -lobed wrinkle in the interval  $x \in [-l_1/2, l_1/2]$  can be expressed as

$$w_m(x) = \frac{A_m}{2} \left[ 1 + \cos \left( \frac{2\pi x}{l_m} - q\pi \right) \right] \quad (1)$$

where  $q$  is 0 if  $m$  is odd and is 1 if  $m$  is even. An example is given in Figure 6a where besides a basic, single-lobed wrinkle ( $m = 1$ , black line) we also show wrinkles having two ( $m = 2$ , red line) and three ( $m = 3$ , blue line) lobes. In order to be able to directly compare wrinkles containing different numbers of lobes, the total length of wrinkled graphene in the model is kept constant. This condition in turn yields the periods and amplitudes of multi-lobed wrinkles:  $l_m = l_1/m$  and  $A_m = A_1/m$  (cf. Figure 6a, see Supplementary data for details).

As the total delaminated graphene length in the model is the same in all profiles, the strain within graphene and the accompanying strain energy do not change for different profiles. Thus, the profitability of multiple lobes depends only on the balance between the unfavorable bending energy cost and the favorable van der Waals binding energy gained in the areas where graphene is brought close to iridium. In principle, additional energy can also be gained from the van der Waals interaction between the neighboring lobes [18]. However, for typical profiles considered here, this contribution is negligible and is not taken into account. We model the van der Waals energy of the profile by summing the Lenard-Jones 6-12 interactions between the atoms in the graphene and iridium, so that the binding energy per unit area of the profile is given by [57]

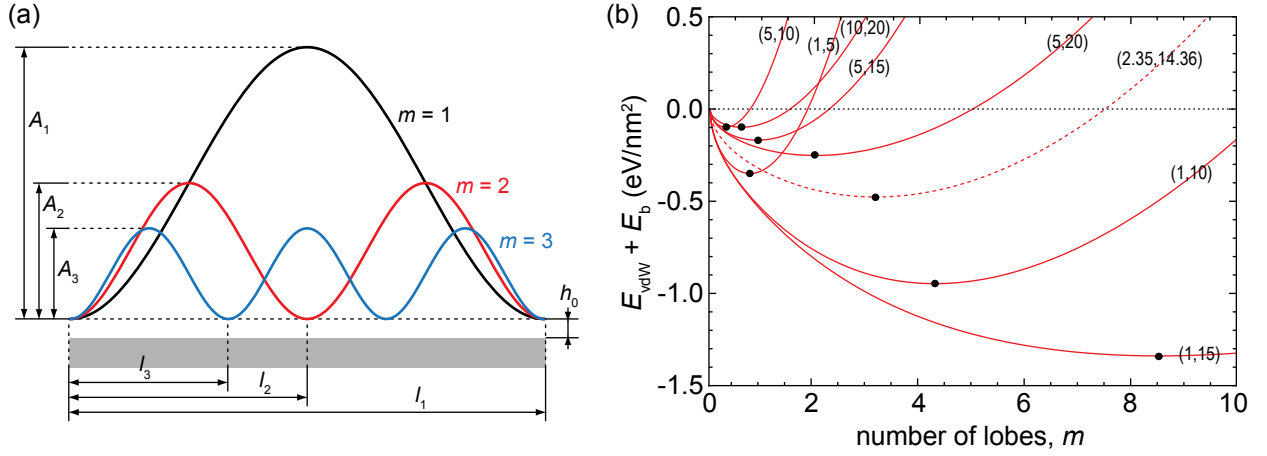


Figure 6. (a) Cross-sections of multi-lobed wrinkles for  $m = 1, 2$  and  $3$  (see text for details).  $h_0$  is the equilibrium graphene-substrate separation. (b) The sum of binding and bending energies of a wrinkle per unit area as a function of number of lobes within a wrinkle. Energy minima are found for different number of lobes, as indicated by black dots. The numbers in brackets correspond to  $(A_1, l_1) = (mA_m, ml_m)$  in nanometers and optimal  $m$  is determined for each curve from the position of its minimum. The red dashed curve is plotted in accordance with the parameters obtained from the STM data shown in Figure 7.

$$E_{vdW} = -\frac{\gamma}{l_1} \int_{-l_1/2}^{l_1/2} \left[ \frac{3}{2} \left( \frac{h_0}{w_m(x) + h_0} \right)^3 - \frac{1}{2} \left( \frac{h_0}{w_m(x) + h_0} \right)^9 \right] dx, \quad (2)$$

where  $h_0$  is the equilibrium graphene-iridium separation which is set to  $3.4 \text{ \AA}$  [41], and  $\gamma$  is the graphene-iridium (111) binding energy per unit area of a flat graphene; it amounts to  $50 \text{ meV per C atom}$  ( $0.308 \text{ J/m}^2$ ) [41]. The bending energy per unit area is given by [58]

$$E_b = \frac{D}{2l_1} \int_{-l_1/2}^{l_1/2} \left( \frac{d^2 w_m(x)}{dx^2} \right)^2 dx, \quad (3)$$

where  $D$  is the graphene bending rigidity having a value of  $0.238 \text{ nN}\cdot\text{nm}$  [47, 54, 57]. The comparison of the total energy  $E_{vdW} + E_b$  for different number of lobes  $m$  is shown in Figure 6b for several combination of the parameters  $(A_1, l_1) = (mA_m, ml_m)$  (additional details of the calculation are given in the Supplementary data). Black dots mark the minima of the displayed curves. The graph shows that for certain combinations of  $l_1$  and  $A_1$  it is energetically more favorable to form multi-lobed wrinkles. For example, a single-lobed wrinkle with  $A_1 = 5 \text{ nm}$  and  $l_1 = 20 \text{ nm}$  [cf. (5, 20) curve in Figure 6b] is less preferable than a wrinkle containing the same amount of graphene but having two lobes so that its amplitude and wavelength are  $A_2 = A_1/2 = 2.5 \text{ nm}$  and  $l_2 = l_1/2 = 10 \text{ nm}$ , respectively. In general, multi-lobed wrinkles become preferable when the width of a wrinkle is much larger than its amplitude. In such cases, energy gained by additional binding of graphene to iridium upon forma-

tion of several lobes compensates for the cost of graphene bending.

The multi-lobed wrinkle structures are observed for Gr/Ir(111). Figure 7a shows a constant-current topographic STM image of a wrinkle, indicating the existence of several lobes. In order to resolve the structure in more detail, first derivative of the topographic image is shown in Figure 7b. Additionally, Figure 7c shows the wrinkle profile (taken along the red line in Figure 7a) where we identify four separate lobes as schematically indicated by a dashed line. In our STM experiments such complex wrinkle profile was often found. Possible multiple-tip effects are eliminated on the basis of the observation that multi-lobed structures are observed in joining wrinkles protruding in different directions (cf. Figure 5c), thus regardless of the scanning direction. Moreover, images of surrounding flat areas do not give any indication of multiple-tip imaging. The measured topographic wrinkle profile does not match our model from Figure 6 ideally. One should take into account, however, that our model profile is a variational *ansatz* used only to demonstrate the propensity towards formation of multi-lobed wrinkle profiles. As such, it is not an exact solution of the problem, and its comparison with the experiments should be performed with care. In addition, the finite radius of the STM tip may not allow for clear imaging of narrow trenches in between the individual lobes. Furthermore, during STM imaging of such curved structures

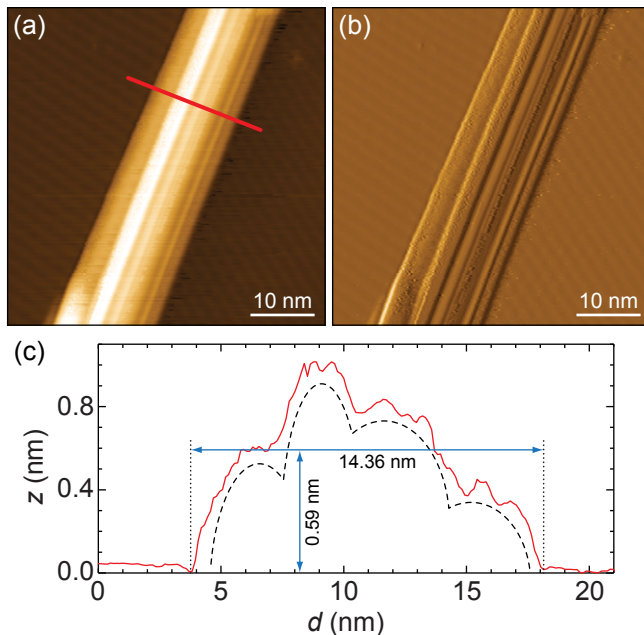


Figure 7. STM measurements of multi-lobed wrinkle. Topography is shown in (a) and the corresponding first derivative is shown in (b). Panel (c) shows a profile across the red line in (a) where four lobes are identified as schematically indicated by black dotted line. Blue arrows mark total width and average height of the wrinkle. Tunneling voltage: 630 mV, tunneling current: 2 nA.

an increased contributions to the tunneling current from the side of the STM tip can be expected, which can affect the measured topographic profile. One should note, however, that the experimentally determined lobes have similar widths, in reasonable agreement with the model calculation which assumes the same widths for all the lobes.

Total width of the wrinkle is 14.36 nm whereas the height is estimated to be 0.59 nm on the basis of its average out-of-plane displacement (cf. blue arrows in Figure 7c). In Figure 6b, the red dashed line corresponds to these experimental values:  $l_1 = 14.36$  nm and  $A_1 = 4 \cdot A_4 = 2.35$  nm. Minimum of the curve is found at  $m \approx 3$ , which is in rough agreement with four lobes inferred from the STM data. At this point we would like to highlight two important virtues of our model: (i) it predicts multi-lobed wrinkles, and (ii) it does so in a semi-quantitative fashion, as can be seen from the anticipated number of lobes for the wrinkle shown in Figure 7.

An issue which remains to be explained is the appearance of several lobes in a profile of a single wrinkle. Namely, lobes could be conceptually separated from each other forming thus several single-lobed wrinkles which would have the same energy as a multi-lobed wrinkle. However, whereas this would indeed be the case for parallel wrinkles in essentially 1D model considered here,

the inclusion of separated lobes in the already formed, connected two-dimensional WN would require additional energy to form new wrinkle junctions. The fact that we do observe multi-lobed wrinkles suggests also the scenario for their formation. As the temperature is lowered, at a transition temperature the strain in the graphene relaxes through the formation of, likely, single-lobed wrinkles. The transition from a flat graphene to a WN is not instantaneous (see the movie clip in the Supplementary data), as there is disorder in the system (it is thus difficult to speak of a well-defined critical temperature for wrinkle formation). As the temperature is further lowered, the existing wrinkles grow, the new ones form, and they soon connect to each other forming the WN with many junctions. Upon further temperature decrease, additional strain accumulates. Its relaxation may proceed either by formation of new wrinkles, by repositioning of the existing wrinkles or by influx of graphene in the already formed WN, increasing thus both wrinkle amplitude and width. Although a different network topology may be energetically preferred at lower temperatures, its formation would require a global reconstruction of the established WN, so that the additional strain relaxes in the already formed network. The dynamical scenario that we propose indicates that the topological properties of the network are fixed in some interval of elevated temperature required to form most of the wrinkle junctions. The once formed network frustrates the system at lower temperatures, the wrinkle junctions behaving as rigid anchors, and the strain relaxes only by increase of the width and amplitude of the wrinkle profiles in the network established at elevated temperature. The influx of graphene in the wrinkle profiles with the lowering of the temperature induces the formation of multiple lobes. The frustration of the WN is also consistent with the observed hysteretic behavior in the heating and cooling cycles.

Even though they were not discussed in the existing literature in detail, wrinkles exhibiting multiple lobes were also observed in transferred graphene grown on Cu foils [18]. In that case, wrinkles are found in a broad range of widths. For wide wrinkles, wrinkle height is approximately constant and relatively low ( $\sim 1$  nm), whereas for narrow wrinkles it is several times larger ( $\sim 2 - 6$  nm). This observation can be explained with the aid of our model: wide wrinkles tend to form multi-lobed structures (wider wrinkle  $\Rightarrow$  larger number of lobes) which is reflected in their constant height. Moreover, the accompanying AFM measurements of wrinkle profiles provide strong indication of a presence of several sequential lobes within wide wrinkles. The concept of competition between binding and bending energies in wrinkling phenomena is also valid for other layered van der Waals materials. It was recently shown that the out-of-plane deviations found in MoS<sub>2</sub> layers exhibit configurations similar to multi-lobed wrinkles which are stable only if



the total width of such structures is sufficiently large [22]. In the case when separation between individual lobes is reduced, they merge and form a single-lobed wrinkle due to the lower cost of bending energy.

#### IV. CONCLUSION

For the R0 graphene, the WN exhibits quasi-hexagonal ordering with wrinkles extending in three preferential directions aligned with the dense-packed atomic rows of the Ir(111) surface. Such ordering is absent in the R30 graphene due to the reduced graphene-iridium binding. We find that the WN can be well approximated by the VD which greatly facilitates its description and parametrization. The formation of wrinkles at elevated temperatures is accompanied by an increase of LEEM reflectivity in their immediate vicinity and we propose that the reason for this is localized, inhomogeneous stress relaxation of the graphene lattice. Moreover, structural features of iridium or graphene, such as wrinkles themselves or dirt particles, can act as nucleation sites for other wrinkles. Finally, our STM results and model calculation indicate that multi-lobed wrinkle profiles are energetically stable and result from the frustration of the WN during sample cooldown. Our study brings new insights into the properties of wrinkles and WN in epitaxial graphene and is of potential use in special electronic, optical or mechanical applications of graphene and follow-up materials.

#### ACKNOWLEDGMENTS

The financial support by the Unity Through Knowledge Fund (Grant No. 66/10) is gratefully acknowledged. Research has been carried out in part at the Center for Functional Nanomaterials and National Synchrotron Light Source, BNL, which are supported by the U.S. Department of Energy, Office of Basic Energy Sciences, under Contracts No. DE-AC02-98CH10886 and DE-SC0012704. The financial support through the Center of Excellence for Advanced Materials and Sensing Devices, research unit for Graphene and Related 2D Structures is gratefully acknowledged.

#### APPENDIX A. SUPPLEMENTARY DATA

Supplementary data associated with this article can be found, in the online version, at <http://dx.doi.org/10.1016/j.carbon.2015.07.059>.

#### REFERENCES

- 
- \* mpetrovic@ifs.hr
- [1] F. Schwierz, *Nat. Nanotechnol.* **5**, 487 (2010).
  - [2] F. Bonaccorso, Z. Sun, T. Hasan, and A. C. Ferrari, *Nat. Photonics* **4**, 611 (2010).
  - [3] D. A. C. Brownson, D. K. Kampouris, and C. E. Banks, *J. Power Sources* **196**, 4873 (2011).
  - [4] S. Bae, H. Kim, Y. Lee, X. Xu, J.-S. Park, Y. Zheng, *et al.*, *Nat. Nanotechnol.* **5**, 574 (2010).
  - [5] A. H. Castro Neto, F. Guinea, N. M. R. Peres, K. S. Novoselov, and A. K. Geim, *Rev. Mod. Phys.* **81**, 109 (2009).
  - [6] O. V. Yazyev and Y. P. Chen, *Nat. Nanotechnol.* **9**, 755 (2014).
  - [7] P. Sutter, J. T. Sadowski, and E. Sutter, *Phys. Rev. B* **80**, 245411 (2009).
  - [8] S. J. Chae, F. Güneş, K. K. Kim, E. S. Kim, G. H. Han, S. M. Kim, *et al.*, *Adv. Mater.* **21**, 2328 (2009).
  - [9] A. N. Obraztsov, E. A. Obraztsova, A. V. Tyurnina, and A. A. Zolotukhin, *Carbon* **45**, 2017 (2007).
  - [10] A. T. N'Diaye, R. Van Gastel, A. J. Martínez-Galera, J. Coraux, H. Hattab, D. Wall, *et al.*, *New J. Phys.* **11**, 113056 (2009).
  - [11] E. Loginova, S. Nie, K. Thürmer, N. C. Bartelt, and K. F. McCarty, *Phys. Rev. B* **80**, 085430 (2009).
  - [12] X. Li, W. Cai, J. An, S. Kim, J. Nah, D. Yang, *et al.*, *Science* **324**, 1312 (2009).
  - [13] M. Liu, Y. Zhang, Y. Chen, Y. Gao, T. Gao, D. Ma, *et al.*, *ACS Nano* **6**, 10581 (2012).
  - [14] L. B. Biedermann, M. L. Bolen, M. A. Capano, D. Zemlyanov, and R. G. Reifengerger, *Phys. Rev. B* **79**, 125411 (2009).
  - [15] G. F. Sun, J. F. Jia, Q. K. Xue, and L. Li, *Nanotechnology* **20**, 355701 (2009).
  - [16] G. Prakash, M. A. Capano, M. L. Bolen, D. Zemlyanov, and R. G. Reifengerger, *Carbon* **48**, 2383 (2010).
  - [17] M. Lanza, Y. Wang, A. Bayerl, T. Gao, M. Porti, M. Nafria, *et al.*, *J. Appl. Phys.* **113**, 104301 (2013).
  - [18] W. Zhu, T. Low, V. Perebeinos, A. A. Bol, Y. Zhu, H. Yan, *et al.*, *Nano Lett.* **12**, 3431 (2012).
  - [19] K. Xu, P. Cao, and J. R. Heath, *Nano Lett.* **9**, 4446 (2009).
  - [20] L. Gao, W. Ren, H. Xu, L. Jin, Z. Wang, T. Ma, *et al.*, *Nat. Commun.* **3**, 699 (2012).
  - [21] K. K. Kim, A. Hsu, X. Jia, S. M. Kim, Y. Shi, M. Hofmann, *et al.*, *Nano Lett.* **12**, 161 (2012).
  - [22] A. Kushima, X. Qian, P. Zhao, S. Zhang, and J. Li, *Nano Lett.* **15**, 1302 (2015).
  - [23] Y. Mei, D. J. Thurmer, F. Cavallo, S. Kiravittaya, and O. G. Schmidt, *Adv. Mater.* **19**, 2124 (2007).
  - [24] B. Li, Y.-P. Cao, X.-Q. Feng, and H. Gao, *Soft Matter* **8**, 5728 (2012).
  - [25] O. V. Yazyev and S. G. Louie, *Nat. Mater.* **9**, 806 (2010).
  - [26] S. Chen, Q. Li, Q. Zhang, Y. Qu, H. Ji, R. S. Ruoff, *et al.*, *Nanotechnology* **23**, 365701 (2012).
  - [27] D. Srivastava, D. W. Brenner, J. D. Schall, K. D. Ausman, M. Yu, and R. S. Ruoff, *J. Phys. Chem. B* **103**, 4330 (1999).

- [28] E. Starodub, N. C. Bartelt, and K. F. McCarty, *J. Phys. Chem. C* **114**, 5134 (2010).
- [29] Y. Zhang, Q. Fu, Y. Cui, R. Mu, L. Jin, and X. Bao, *Phys. Chem. Chem. Phys.* **15**, 19042 (2013).
- [30] F. S. Khokhar, G. Hlawacek, R. Van Gastel, H. J. W. Zandvliet, C. Teichert, and B. Poelsema, *Surf. Sci.* **606**, 475 (2012).
- [31] M. Petrović, I. Šrut Rakić, S. Runte, C. Busse, J. T. Sadowski, P. Lazić, *et al.*, *Nat. Commun.* **4**, 2772 (2013).
- [32] S. Schumacher, F. Huttmann, M. Petrović, C. Witt, D. F. Förster, C. Vo-Van, *et al.*, *Phys. Rev. B* **90**, 235437 (2014).
- [33] S. Vlaic, A. Kimouche, J. Coraux, B. Santos, A. Locatelli, and N. Rougemaille, *Appl. Phys. Lett.* **104**, 101602 (2014).
- [34] A. Kimouche, O. Renault, S. Samaddar, C. Winkelmann, H. Courtois, O. Fruchart, *et al.*, *Carbon* **68**, 73 (2014).
- [35] J. Zang, S. Ryu, N. Pugno, Q. Wang, Q. Tu, M. J. Buehler, *et al.*, *Nat. Mater.* **12**, 321 (2013).
- [36] Z. Pan, N. Liu, L. Fu, and Z. Liu, *J. Am. Chem. Soc.* **133**, 17578 (2011).
- [37] K. Kim, Z. Lee, B. D. Malone, K. T. Chan, B. Alemán, W. Regan, *et al.*, *Phys. Rev. B* **83**, 245433 (2011).
- [38] J. Coraux, A. T. N'Diaye, C. Busse, and T. Michely, *Nano Lett.* **8**, 565 (2008).
- [39] I. Pletikosić, M. Kralj, P. Pervan, R. Brako, J. Coraux, A. T. N'Diaye, *et al.*, *Phys. Rev. Lett.* **102**, 056808 (2009).
- [40] M. Kralj, I. Pletikosić, M. Petrović, P. Pervan, M. Milun, A. T. N'Diaye, *et al.*, *Phys. Rev. B* **84**, 075427 (2011).
- [41] C. Busse, P. Lazić, R. Djemour, J. Coraux, T. Gerber, N. Atodiresei, *et al.*, *Phys. Rev. Lett.* **107**, 036101 (2011).
- [42] S. Runte, P. Lazić, C. Vo-Van, J. Coraux, J. Zegenhagen, and C. Busse, *Phys. Rev. B* **89**, 155427 (2014).
- [43] H. Hattab, A. T. N'Diaye, D. Wall, C. Klein, G. Jnawali, J. Coraux, *et al.*, *Nano Lett.* **12**, 678 (2012).
- [44] J. Coraux, A. T. N'Diaye, M. Engler, C. Busse, D. Wall, N. Buckanie, F. J. Meyer Zu Heringdorf, *et al.*, *New J. Phys.* **11**, 023006 (2009).
- [45] I. Horcas, R. Fernández, J. M. Gómez-Rodríguez, J. Colchero, J. Gómez-Herrero, and A. M. Baro, *Rev. Sci. Instrum.* **78**, 013705 (2007).
- [46] A. T. N'Diaye, J. Coraux, T. N. Plasa, C. Busse, and T. Michely, *New J. Phys.* **10**, 043033 (2008).
- [47] Q. Lu, M. Arroyo, and R. Huang, *J. Phys. D: Appl. Phys.* **42**, 102002 (2009).
- [48] E. Starodub, A. Bostwick, L. Moreschini, S. Nie, F. Gabaly, K. McCarty, *et al.*, *Phys. Rev. B* **83**, 125428 (2011).
- [49] A. Okabe, B. Boots, K. Suhihara, and S. N. Chiu, *Spatial Tessellations: Concepts and Applications of Voronoi Diagrams*, 2nd ed. (Wiley, Chichester, 1992).
- [50] H. Honda, *Int. Rev. Cytol.* **81**, 191 (1983).
- [51] H. J. Hilhorsta, *Eur. Phys. J. B* **64**, 437 (2008).
- [52] K. Zhang and M. Arroyo, *J. Mech. Phys. Solids* **72**, 61 (2014).
- [53] J. A. Robinson, C. P. Puls, N. E. Staley, J. P. Stitt, M. A. Fanton, K. V. Emtsev, *et al.*, *Nano Lett.* **9**, 964 (2009).
- [54] K. Zhang and M. Arroyo, *J. Appl. Phys.* **113**, 193501 (2013).
- [55] F. Cleymand, C. Coupeau, and J. Grilhé, *Scr. Mater.* **44**, 2623 (2001).
- [56] D. Vella, J. Bico, A. Boudaoud, B. Roman, and P. M. Reis, *Proc. Natl. Acad. Sci. U. S. A.* **106**, 10901 (2009).
- [57] Z. H. Aitken and R. Huang, *J. Appl. Phys.* **107**, 123531 (2010).
- [58] S. Timoshenko and S. Woinowsky-Krieger, *Theory of Plates and Shells*, 2nd ed. (McGraw-Hill, New York, 1959).